

Quantum simulator of an open quantum system using superconducting qubits: exciton transport in photosynthetic complexes

Sarah Mostame¹, Patrick Rebentrost¹, Alexander Eisfeld¹, Andrew J. Kerman² Dimitris I. Tsomokos³, and Alán Aspuru-Guzik*¹

¹*Department of Chemistry and Chemical Biology,
Harvard University, Cambridge, Massachusetts 02138, USA*

²*Lincoln Laboratory, Massachusetts Institute of Technology, Lexington, Massachusetts, 02420, USA*

³*Department of Mathematics, Royal Holloway, University of London, Egham, TW20 0EX, United Kingdom*

Open quantum system approaches are widely used in the description of physical, chemical and biological systems. A famous example is electronic excitation transfer in the initial stage of photosynthesis, where harvested energy is transferred with remarkably high efficiency to a reaction center. This transport is affected by the motion of a structured vibrational environment, which makes simulations on a classical computer very demanding. Here we propose an analog quantum simulator of complex open system dynamics with a precisely engineered quantum environment. Our setup is based on superconducting circuits, a well established technology. As an example, we demonstrate that it is feasible to simulate exciton transport in the Fenna-Matthews-Olson photosynthetic complex. Our approach allows for a controllable single-molecule simulation and the investigation of energy transfer pathways as well as non-Markovian noise-correlation effects.

Understanding strongly interacting quantum systems with many degrees of freedom is one of the big challenges in physics and chemistry [1]. Classical computational methods are restricted by exponentially increasing amount of resources required for the simulations. Quantum computers are conjectured to be a possible solution as the resources to simulate arbitrary quantum systems grow polynomially with the size of the system under study [2, 3]. However, universal quantum computers of sufficient size and performance are not available yet, one of the big problems being the loss of quantum mechanical coherence, i.e., decoherence [4]. Designing a special quantum system in the laboratory, which mimics the quantum dynamics of a particular model of interest, see for example, Refs. [5–10], can be a more viable alternative to an all-purpose quantum computer.

Here we propose a quantum simulator architecture using superconducting quantum bits (qubits) that is capable of simulating complex open quantum systems using currently-available technology in realizable parameter ranges. We will focus on the Fenna-Matthews-Olson (FMO) pigment-protein complex on a single molecule level. The recent observations [11, 12] of quantum beatings and long-lived quantum coherence in several photosynthetic light-harvesting complexes, such as the FMO complex in the green sulfur bacterium *Chlorobium tepidum* or the reaction center of the purple bacterium *Rhodobacter sphaeroides*, suggest possible evidence that quantum effects give rise to the high energy transport efficiency found for these complexes. There is a remarkable amount of recent theoretical research related to the question of the molecular structure, vibrational environment, the origin and the role of long-lived quantum coherences [13–23]. The electronic degrees of freedom are coupled to a finite temperature vibrational environment and the dynamics of the relevant electronic system can be studied by means of open quantum system approaches. In

quantum computing, the focus of much of the research has been on reducing the magnitude and influence of environmental decoherence and dissipation. However, controlled coupling to a dissipative environment can also be exploited [24–26]. In this work, we focus on *engineering* the decoherence to simulate open quantum systems that are challenging to study using classical computers.

We propose two approaches for simulating the vibrational environment. The first approach is based on engineering a classical noise source such that it represents the atomistic fluctuations of the protein environment. A prototypical experiment of environment-assisted quantum transport (ENAQT) can be performed [16]. The second approach allows for the precise engineering of the complex non-Markovian environment, i.e., an environment that has long-term memory. This is achieved by the explicit coupling of quantum inductor-resistor-capacitor (LRC) oscillators to the qubits which allows for energy and coherence exchange between the resonators and the qubits. Both approaches are based on present-day superconducting qubit implementations. Fabrication of superconducting circuitry is done by several research labs. We focus here on flux qubits, where two-qubit coupling was shown to be sign- and magnitude-tunable [27, 28] and methods of scaling to a moderate number of qubits have been discussed in Refs [29, 30]. We show that realistic simulation of photosynthetic energy transfer is feasible with current superconducting circuit devices.

I. THE MODEL HAMILTONIAN

We are interested in the dynamics of a finite dimensional system which is linearly coupled to a bath of harmonic oscillators. In the following we refer to the system as “electronic system” and to the quantum environment as “phonon bath” or “vibrational environment”. The

corresponding total Hamiltonian is written as

$$H_{\text{tot}} = H_{\text{el}} + H_{\text{ph}} + H_{\text{el-ph}}. \quad (1)$$

A. The system

We are often (e.g., in the FMO complex) interested in the transfer of a single electronic excitation. Thus basis states $|j\rangle$ are defined by the electronic excitation residing on molecule (site) j and all other sites being in their electronic ground state. The electronic Hamiltonian in this site basis is given by $H_{\text{el}} = \sum_{j=1}^N \tilde{\varepsilon}_j |j\rangle \langle j| + \sum_{i<j}^N V_{ij} (|i\rangle \langle j| + |j\rangle \langle i|)$, [31]. The diagonal energies $\tilde{\varepsilon}_j$ are identified with the electronic transition energies of site j and the off-diagonal elements V_{ij} are the intermolecular (transition-dipole-dipole) couplings between sites i and j . Different local electrostatic fields of the protein at different sites shift the electronic transition energies [15], resulting in a complicated energy landscape.

B. Coupling to the quantum environment

The vibrational environment is represented by a set of displaced harmonic oscillators. The Hamiltonian of the phonon bath is written as $H_{\text{ph}} = \sum_{j=1}^N H_{\text{ph}}^j$, where $H_{\text{ph}}^j = \sum_{\ell} \hbar \omega_{\ell}^j (a_{\ell}^{j\dagger} a_{\ell}^j + 1/2)$ with $a_{\ell}^{j\dagger}$ (a_{ℓ}^j) being the creation (annihilation) operator of excitations in the ℓ -th bath mode of site j . In the present work we restrict to the situation where each site has its own phonon environment which is uncorrelated with the phonon modes at the other sites. This is motivated by recent results obtained for the FMO complex [32, 33]. The diagonal part of the electronic Hamiltonian couples linearly to the phonon modes. The electron-phonon coupling term can be written as

$$H_{\text{el-ph}} = \sum_{j=1}^N H_{\text{el-ph}}^j = \sum_{j=1}^N |j\rangle \langle j| \left[\sum_{\ell} \chi_{j\ell} (a_{\ell}^{j\dagger} + a_{\ell}^j) \right]. \quad (2)$$

Here $\chi_{j\ell} = \hbar \omega_{\ell}^j d_{j\ell}$ is the coupling between the j -th site and the ℓ -th phonon mode with ω_{ℓ}^j being the frequency of the ℓ -th phonon mode coupled to the j -th site and $d_{j\ell}$ is the dimensionless displacement of the minima of the ground and excited state potentials of the ℓ -th phonon mode at site j . Notice that the so-called reorganization energy $\lambda_j \equiv \sum_{\ell} \hbar \omega_{\ell}^j d_{j\ell}^2 / 2$ was implicitly included in the above electronic transition energy $\tilde{\varepsilon}_j = \varepsilon_j + \lambda_j$, with ε_j being the energy difference of the minima of the potential energy surfaces for site j , see Figure 1 (a) and the Supporting Information for more details.

It is known that complete information about the effect of the environment on a quantum system is determined

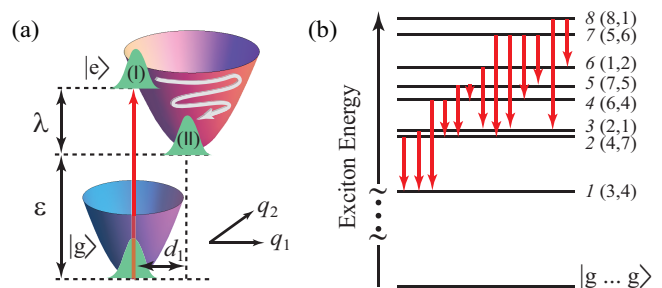


FIG. 1. (a) Model of exciton-phonon dynamics in a system with two electronic states $|g\rangle$ and $|e\rangle$ and two dissipative vibrational modes q_1 and q_2 . After a vertical Franck-Condon electronic excitation the phonon degrees of freedom are in a non-equilibrium position (I) from which the system relaxes to the displaced equilibrium configuration in the excited state (II). The displacements are given by d_1 and d_2 and the energy scale associated with this relaxation is the reorganization energy λ . This vibrational reorganization is not captured in most Markovian models. (b) Energy levels of the electronic Hamiltonian for the FMO complex denoted by $M(i, j)$, where (i, j) indicate the two most significant BChl pigments participating in the delocalized excitonic states M . The red arrows indicate the dominant pathways for the energy transport based on Redfield theory [17].

by the spectral density (SD) function [34], which is defined by

$$J_j(\omega) = \sum_{\ell} |\chi_{j\ell}|^2 \delta(\omega - \omega_{j\ell}) \quad (3)$$

for site j . Due to the high number of modes of the environment, $J_j(\omega)$ can be considered as a continuous function of ω . To account for finite temperature, we transform the spectral density [35, 36] $C_j(\omega, T) = \{1 + \coth[\hbar\omega/(2k_B T)]\} J_j^A(\omega)$, where the subscript ‘‘A’’ denotes the antisymmetric spectral density $J_j^A(\omega) = J_j(\omega)$ if $\omega \geq 0$; and $J_j^A(\omega) = -J_j(-\omega)$ if $\omega < 0$. The spectral density $C_j(\omega, T)$ fulfills the detailed balance condition [35] and we name it ‘‘temperature-dependent spectral density’’.

It turns out that the relevant spectral densities of our problem can be approximated by a finite number of broadened peaks. These broadened peaks can often be associated with the vibrational modes of the molecules. Upon electronic excitation of a molecule, the vibronic Gaussian wavepacket of the ground state is projected into a displaced wavepacket in the excited state at the Franck-Condon point, see Figure 1 (a). The nuclei wavepacket then moves on the excited state potential energy surface and reorganizes to the minimum point while the reorganization energies of the respective modes are dissipated.

Finally, to facilitate the comparison with flux qubits

we rewrite the total Hamiltonian 1 using Pauli matrices

$$\begin{aligned}
H_{\text{tot}} = & \frac{1}{2} \sum_{j=1}^N \tilde{\varepsilon}_j \sigma_z^j + \frac{1}{2} \sum_{i<j}^N V_{ij} (\sigma_x^i \sigma_x^j + \sigma_y^i \sigma_y^j) \\
& + \sum_{j=1}^N \sum_{\ell} \hbar \omega_{\ell}^j \left(a_{\ell}^{j\dagger} a_{\ell}^j + \frac{1}{2} \right) \\
& + \sum_{j=1}^N \sum_{\ell} \chi_{j\ell} \sigma_z^j \left(a_{\ell}^{j\dagger} + a_{\ell}^j \right). \quad (4)
\end{aligned}$$

Expressing the above Hamiltonian in the system energy eigenbasis, defined by $H_{\text{el}} |M\rangle = E_M |M\rangle$, we have $H_{\text{tot}} = \sum_M E_M |M\rangle \langle M| + \sum_{M,N,\ell} \mathcal{K}_{MN}^{\ell} |M\rangle \langle N| (a_{\ell}^{j\dagger} + a_{\ell}^j) + H_{\text{ph}}$ with $\mathcal{K}_{MN}^{\ell} = \sum_j \langle M|j\rangle \langle j|N\rangle \chi_{j\ell}$. This shows that the system-bath coupling is off-diagonal in the eigenbasis.

C. The classical noise approximation

Although the main goal of the present paper is to simulate the fully quantum mechanical Hamiltonian 4, it is also useful to consider the much simpler (but important) case where the quantum environment is replaced by time-dependent fluctuations of the transition energies. This is the basis of the often employed Haken-Strobl-Reineker (HSR) model for excitation transfer [37]. Furthermore, atomistic MD/QM/MM simulations [32, 33] can readily provide noise time-series. In the classical noise approach, the system dynamics is obtained by averaging over many trajectories with the time-dependent Hamiltonian

$$\tilde{H}_{\text{tot}} = \frac{1}{2} \sum_{j=1}^N [\tilde{\varepsilon}_j + \delta\tilde{\varepsilon}_j(t)] \sigma_z^j + \frac{1}{2} \sum_{i<j}^N V_{ij} (\sigma_x^i \sigma_x^j + \sigma_y^i \sigma_y^j), \quad (5)$$

where the influence of the environment is solely contained in the time-dependent site energy fluctuations $\delta\tilde{\varepsilon}_j(t)$. Often, as in the HSR model, it is assumed that the fluctuations are uncorrelated Gaussian white noise.

II. THE FMO COMPLEX

The model Hamiltonian 1 can be used to describe a single excitation in the FMO complex. The FMO complex acts as a highly efficient excitation wire, transferring the energy harvested by the photosynthetic antennae to a reaction center. The FMO trimer has a trimeric structure exhibiting C_3 -symmetry and each of the monomers consists of a network of eight [23] bacteriochlorophyll a (BChl a) pigment molecules. Since the coupling between monomers is very small and can be neglected on the time-scales of interest, we focus on a single monomer in the following. The BChl pigments in the monomer are surrounded by a protein environment. Conformational

motions of this protein environment (static disorder) are slow compared to the timescale of interest and affect energy levels of the pigments by electrostatic interaction [15]. The ranges of site energy differences $|\tilde{\varepsilon}_i - \tilde{\varepsilon}_j|$ and couplings V_{ij} are given in table I. These parameters lead to the energy spectrum of the FMO monomer given in Figure 1 (b).

In the present work, we consider two spectral densities relevant to the FMO complex. First, a model super-Ohmic SD [14], $J(\omega) = \lambda (\omega/\omega_c)^2 \exp(-\omega/\omega_c)$ with reorganization energy $\lambda = 35 \text{ cm}^{-1}$ and cutoff frequency $\omega_c = 150 \text{ cm}^{-1}$, shown as the transformed $C(\omega, T)$ by the blue dashed line in Figure 4 (a). We have dropped the subscript j under the assumption that all 8 sites have same spectral density and reorganization energy. Second, the experimental spectral density [14, 38] shown by blue dashed line in Figure 4 (b). Notice that it is very challenging to simulate the experimental SD with current computational methods because of the apparent peaks, see Figure 4 (b), and the mixing of vibrational dynamics caused by the electronic interaction between the sites. This structured spectral density with strong peaks is expected to lead to strong non-Markovian behavior.

In the biological situation, the FMO complex most likely obtains the excitation at sites 1, 6, or 8, since these BChls are close to the chlorosomal antennas, where photons are absorbed. It is often assumed that this excitation is initially local to these sites. Low energy site 3 is the target site for the excitation and is close to the reaction center where further biochemical processes take place. In the ultrafast experiments, broad laser pulses excite a superposition of several delocalized exciton states.

III. THE SIMULATOR

It is challenging to simulate the open quantum system described in the previous section on conventional computers [20, 36, 39], even using modern parallel processing units [40–42]. Here we propose using flux qubits coupled with tunable flux-flux couplings for this task. The environment is modeled by classical noise or quantum oscillators coupled to the flux qubits.

A. The system Hamiltonian

Consider first a single flux qubit. The relevant quantum states are the ones with magnetic flux pointing up $|\uparrow\rangle$ and down $|\downarrow\rangle$ or, equivalently, opposite directions of persistent current along the loop. In this bare basis, the Hamiltonian of a flux qubit is given by $H = (\mathcal{E} \sigma_z + \Delta \sigma_x)/2$, where \mathcal{E} is the energy bias between $|\uparrow\rangle$ and $|\downarrow\rangle$ and Δ is the tunnel splitting between the two states. Here $\mathcal{E} = 2I_p(\phi_x - \phi_0/2)$ [43] with I_p being the persistent current of the qubit and $\phi_0 = h/2e$ being the flux quantum. \mathcal{E} can be tuned to zero to neglect the $\mathcal{E} \sigma_z$ term.

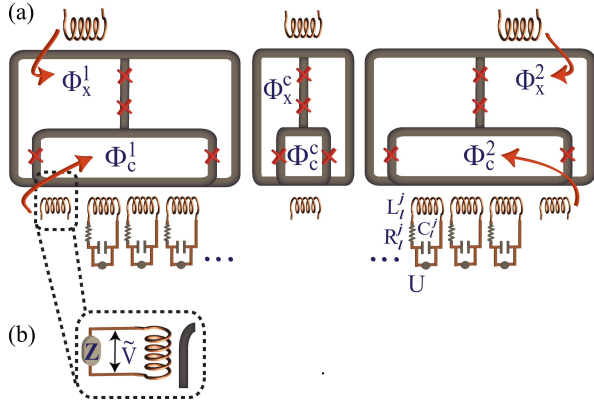


FIG. 2. Circuit diagram of the proposed quantum simulator. (a) The qubit states are encoded in the quantized circulating current of the qubit loop. The red crosses denote Josephson junctions. Two flux qubits are coupled with a tunable $\sigma_z\sigma_z$ -coupling. Each of the qubits is independently coupled to a finite number of quantum LRC oscillators to simulate the non-Markovian vibrational environment. (b) Simulating the vibrational environment by adding a classical noise to each qubit.

A tunable transverse interaction between flux qubits equivalent to that in H_{el} can be realized using additional ‘coupler’ qubits [27, 44]. A schematic of such a simulator is given in Figure 2 (a). The Hamiltonian of the coupled qubit system can be written as $H_q = \sum_{j=1}^N \Delta_j \sigma_x^j / 2 + \sum_{i<j}^N g_{ij}(\Delta_{ij}^c) \sigma_z^i \sigma_z^j$ with $g_{ij}(\Delta_{ij}^c)$ being the coupling strength between flux qubits i and j , which is given by $g_{ij}(\Delta_{ij}^c) \approx \mathcal{J}_{ij} - 2\mathcal{J}_{ic}\mathcal{J}_{jc}/\delta_{ij}$, where Δ_{ij}^c is the (tunable) tunnel splitting of the coupler qubit and we have defined $\delta_{ij} \equiv \Delta_{ij}^c - (\Delta_i + \Delta_j)/2$ and $\mathcal{J}_{mn} \equiv \mathcal{M}_{mn} I_p^m I_p^n$ with $m, n \in i, j, c$ [44]. Here, \mathcal{M}_{mn} is the mutual inductance between qubits m and n . This expression is valid to leading order when $\delta_{ij} \gg |\Delta_i - \Delta_j|, \mathcal{J}_{ic}, \mathcal{J}_{jc}$. Notice that by choosing the magnitude of Δ_{ij}^c to be smaller or larger than $(\Delta_i + \Delta_j)/2$ we can change the sign of the effective coupling. Rewriting the above Hamiltonian in the energy eigenbasis of the qubit $|\pm\rangle = (|\downarrow\rangle + |\uparrow\rangle)/\sqrt{2}$ converts $\sigma_x^j \rightarrow \sigma_z^j$ and $\sigma_z^i \sigma_z^j \rightarrow \sigma_x^i \sigma_x^j \approx (\sigma_x^i \sigma_x^j + \sigma_y^i \sigma_y^j)/2$ in the rotating wave approximation (neglecting strongly off-resonant couplings). This results in

$$H_q \approx \frac{1}{2} \sum_{j=1}^N \Delta_j \sigma_z^j + \frac{1}{2} \sum_{i<j}^N g_{ij}(\Delta_{ij}^c) (\sigma_x^i \sigma_x^j + \sigma_y^i \sigma_y^j), \quad (6)$$

which is of exactly the same form as the system part (first line) of Eq. 4 with Δ_j and $g_{ij}(\Delta_{ij}^c)$ corresponding to $\tilde{\varepsilon}_j$ and V_{ij} , respectively. It is advantageous for the experimental implementation to note that the dynamics of Eqs. 4 and 6 does not depend on absolute site energies $\tilde{\varepsilon}_j$ and Δ_j but only on energy differences $|\tilde{\varepsilon}_i - \tilde{\varepsilon}_j|$ and $|\Delta_i - \Delta_j|$, respectively.

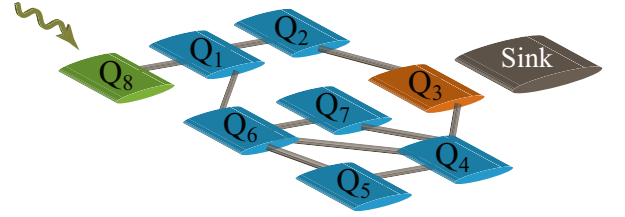


FIG. 3. Experimental layout for simulating the exciton dynamics and environment assisted quantum transport (ENAQT) in the FMO complex (the architecture is based on the interactions given in Ref. [23], where for simplicity of the graphic the couplings below 15 cm^{-1} are not shown). Q_i represent single flux qubits. To simulate a biologically relevant case, one of these qubits, Q_8 shown in green, is prepared initially in the excited state while the others are set to the ground state. The measurement is performed on the target site, Q_3 shown in red. Sinks can be used to trap the energy and quantify the transfer efficiency.

The system of two coupled flux qubits shown in Figure 2 (a) can be extended to eight flux qubits with a special arrangement to simulate eight chlorophylls. An experimental layout simulating the electronic part of the FMO Hamiltonian is given in Figure 3, where Q_j represent flux qubits. Static disorder can be simulated in our proposed scheme by varying the tunnel splittings Δ_j in the flux qubits with each run of the experiment. First all the qubits are in the ground state by simply allowing the system to relax. Then they are initialized in a certain desired initial state to start the dynamics. The excitation of a qubit is straightforward to achieve with the application of a resonant microwave excitation (π -pulse) carried by a microwave line which is connected to the respective qubit. The technique has been used extensively, e.g., for the observation of Rabi oscillations in a flux qubit [43, 45]. After some evolution time the populations of the $|\pm\rangle$ states of the qubits are measured. The measurement is initiated by applying a flux pulse to shift the qubit adiabatically away from $\mathcal{E} = 0$ so that its eigenstates become largely $|\uparrow\rangle$ and $|\downarrow\rangle$ which can be distinguished via the flux induced in a nearby DC SQUID loop. In addition, to capture the effect of reaction centers on the dynamics, we propose to add excitation sinks into the superconducting circuit, see Figure 3. This is done with additional terminated transmission lines or shunt resistors coupled to those sites that are supposed to leak excitations.

B. Engineering classical noise

We will first discuss the more simple case of an environment treated within the classical noise formalism of Eq. 5. We propose two schemes, an active approach and a passive one. The basic idea of both approaches is to simulate the fluctuations of the transition energies by coupling classical noise to the qubits via the flux Φ_c^j ,

see Figure 2 (b). Such a noise affects the tunnel splitting Δ_j in the qubit Hamiltonian. On one hand, the noise can be *actively* created and sent to the qubit by a time-dependent voltage \tilde{V} applied to a control loop [46]. Regarding the *passive* approach, an environmental loop exhibits standard Johnson-Nyquist noise [47]. The bath spectrum $J(\omega)$ of the noise seen by the qubit can be related to the real part of the impedance $Z(\omega)$ [48]: $J(\omega) = K \omega \text{Re}[Z(\omega)]$, with K being a constant depending on the self-inductance of the environment loop and its coupling strength to the flux qubit. With classical circuit design $Z(\omega)$ can be tailored to produce the desired frequency dependence, for example, the ones in Refs. [13, 14, 20]

With simple classical noise a prototypical experiment of ENAQT can be performed [16], see Figure 3. In the FMO complex, the initial state of the simulation can be one of the sites Q_1 , Q_6 , or Q_8 which are close to the antenna in the biological system. Measurement of success of the transport is performed at site Q_3 or by evaluating the population lost to the sink. Such an experiment can show that the environment is not always adversarial, but instead can make certain processes, like quantum transport, more efficient (see the Supporting Information for more details). This transport efficiency should exhibit a maximum at a dephasing rate that corresponds to room temperature in the biological system [16]. Similar ideas of simulating ENAQT have been pursued in [49, 50].

C. Non-Markovian approach

In order to simulate the complex environment described by Eq. 4 and capture the non-Markovian effects, we propose to couple each of the flux qubits inductively to an independent set of a few damped quantum LRC oscillators, see Figure 2 (a). The coupling Hamiltonian between the qubits and oscillators [51] in the energy eigenbasis is given by $H_{q\text{-osc}} = \sum_{j=1}^{N_{\text{LRC}}} \sum_k \eta_{jk} \sigma_z^j (b_k^{j\dagger} + b_k^j)$, with $b_k^{j\dagger}$ (b_k^j) being the creation (annihilation) operator of the k -th oscillator in site j . The coupling strength is given by $\eta_{jk} \equiv \mathcal{M}_{jk} I_0^{jk} (d\Delta_j/d\Phi_c^j)$, where I_0^k is the root mean square (RMS) amplitude of the current in the k -th oscillator ground state.

To simulate the original spectral density 3, we have to design the frequencies and couplings of the oscillators in such a way that the spectral density is reproduced up to a global scaling factor. From the implementation point of view, we are limited to a finite number of oscillators. Thus, we decompose the spectral density of interest into a moderate number of spectral densities of damped oscillators. The spectral density of a single oscillator coupled to a flux qubit can be derived by using a quantum Langevin equation approach [52, 53] and following the detailed balance condition [35]

$$C_{\text{osc}}(\omega, T) = \mathfrak{D} \left[\frac{e^{\hbar\omega/k_B T}}{\kappa^2 + 4(\omega - 2\pi\omega_0)^2} + \frac{1}{\kappa^2 + 4(\omega + 2\pi\omega_0)^2} \right],$$

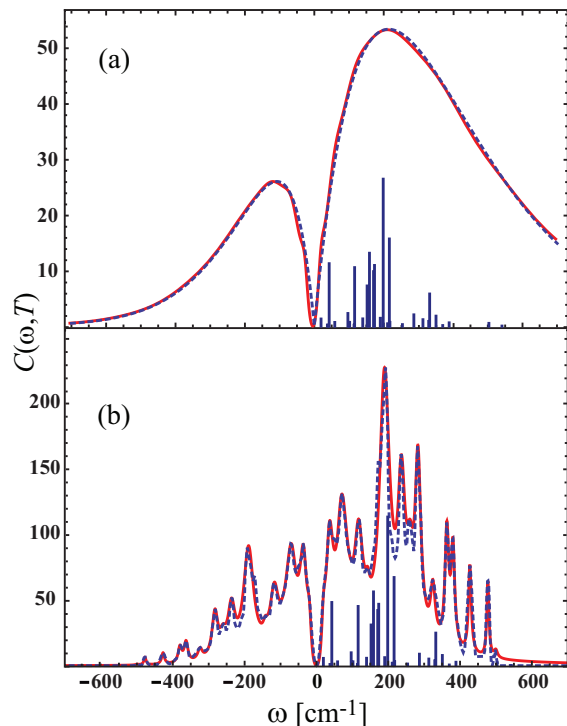


FIG. 4. The parametrization of the temperature-dependent (a) super-Ohmic spectral density and (b) experimental [38] spectral density of the FMO complex into distinct quantum oscillators. The blue dashed lines are the spectral densities and the red solid lines are highly accurate simulation with LRC-oscillators coupled to the flux qubits, see Figure 2 (a). The temperature for both spectral densities is 300 K. The super-Ohmic spectral density is simulated with 6 damped LRC-Oscillators and the experimental one is simulated with 15 damped oscillators. The blue bars show the transition energies [14] for the FMO complex. The obtained parameters are given in the Supporting Information.

where $\mathfrak{D} = (\sqrt{8/\pi} \kappa \eta^2) / (e^{\hbar\omega_0/k_B T} + 1)$ with ω_0 being the transition frequency of the oscillator and η being the coupling strength of the oscillator to the flux qubit. Here, $\kappa = \kappa_0 \exp(-|\omega|/\alpha) \omega^2/\omega_0^2$ with κ_0 being the damping rate and α being a free parameter chosen reasonably to get the desired spectral density. By knowing the above spectral density for the damped quantum oscillators, we first simulate the temperature-dependent super-Ohmic spectral density. At 300 K this spectral density can be simulated with a set of 6 LRC oscillators coupled to each of the flux qubits, see Figure 4 (a), and at 77 K it can be simulated with a set of 7 oscillators (see Figure S1 (a) in the Supporting Information). For the experimental spectral density, we need to couple, for example, 15 oscillators to each qubit, see Figure 4 (b). Notice that the so-obtained SDs in Figure 4 are highly accurate and we can use fewer coupled oscillators if we are interested in less details of the spectral densities. The coupling of the oscillators to the flux qubit results in an additional shift of the qubit tunnel splitting Δ_j due to the reorganiza-

tion energy of the oscillators. This has to be taken into account in the design of the circuit energy landscape.

IV. EXPERIMENTAL FEASIBILITY

The simulation of the time evolution of the FMO complex requires a moderately coherent eight-qubit system, which would be realizable using the flux qubits demonstrated in Ref. [28] and the coupling geometries and methods of Refs. [27, 44]. In the FMO complex the site energies/chlorophyll excitation energies are around 12500 cm^{-1} , with the average site-dependent static shifts of the order of 250 cm^{-1} . We emphasize again that only the *site-energy differences*, not the site energies themselves, play a role in the single-exciton dynamics. The magnitudes of the coupling strengths between the chlorophyll molecules are smaller than 120 cm^{-1} [14]. For superconducting flux qubits, implementable range of the tunnel bias Δ_j is in the range of approximately zero to 13 GHz [28], while the coupling strengths g_{ij} were measured in the range of one GHz to approximately zero [27].

The parameters of the proposed quantum simulator are scaled through the time scale of quantum beatings (τ_{osc}) to be consistent internally as well as with the implementation restrictions, see Table I. Photosynthesis occurs at ambient temperatures, e.g., 300 K, which then maps to 60 mK in superconducting-circuit experiments. The FMO dynamics is usually considered for up to 5 ps, which translates to the timescale of 25 ns in the flux qubits. The energy relaxation time (T_1) of a single qubit has been found [45, 54] to be on the order of a few μs , being a few orders of magnitude larger than the required exciton transfer time. Several coherent beatings between two coupled qubits have been observed [27]. Table I represents the summary of the required range of parameters for the superconducting simulator to imitate the dynamics of the FMO complex.

In simulating the quantum environment of the FMO complex, the required transition frequency of the LRC oscillators are in the range of 120 MHz to 3 GHz and the coupling to the qubits are around 8 MHz to 100 MHz, see Tables S2 and S3 in the Supporting Information. These parameters are experimentally reasonable. The geometry of Figure 3 may cause space problems in implementing this system. To avoid this, the parallel combination of resonators used to implement the desired spectral density can be mapped, for example, to a linear chain of oscillators [55–57], such that only a single resonator would need to be coupled directly to each qubit, see Figure S2 in the Supporting Information. The quality factor (transition frequency/bandwidth) of the quantum oscillators in our proposed simulator are up to 50 or less (i.e., each of the oscillators is strongly overcoupled to an output 50 Ohm line). The coupling to the output line can be tunable to adjust the quality factor of each oscillator in situ. Finally, low-frequency flux noise ($1/f$ noise) is one of the decoherence sources in flux qubits. In our proposal, this

noise is suppressed at the optimal working point [58], where $\mathcal{E} = 0$. All of the above numbers and observations suggest that the site energy differences to coupling ratios of the FMO complex as well as corresponding temperature and environmental couplings are achievable with superconducting circuits.

V. CONCLUSION

We have demonstrated that an appropriately designed network of superconducting qubit-resonator design can simulate not only the coherent exciton transport in photosynthetic complexes, but also the effect of a complicated quantum environment. We have highlighted its experimental feasibility with present-day technology. In particular, we have shown that a straightforward combination of superconducting qubits (representing the chlorophyll molecules) and resonators (simulating the phonon environment) can be used to obtain a reasonable approximation to the exciton and phonon degrees of freedom in the FMO complex. For example, we show ways to engineer a spectral density that reproduces the one of the biological system. One of the advantages of our proposed quantum simulator, compared to the computational methods, is simulating both diagonal and off-diagonal noise. Because of the additional complexity of considering the off-diagonal noise most of the non-Markovian computational methods only take the diagonal noise into the account. Another advantage is that, by design, we have a single molecule setup while all the ultrafast experiments use an ensemble of light harvesting complexes. This allows for more detailed studies of non-Markovian energy transfer pathways.

An important feature of our proposal is the potential to achieve a high level of environment engineering, in such a way that external noise is used to benefit the quantum coherent energy transfer process inside the molecule. However, the broader scope of our work is along the lines of *biomimesis*: the artificial recreation of biological processes, which are already highly optimized through evolution.

ACKNOWLEDGMENTS

The authors are indebted to S. Ashhab, M. Geller, F. Nori, S. Valleau, S. Huelga, and M. H. S. Amin for valuable conversations. We acknowledge DARPA Grant No. N66001-10-1-4063, NIST Award No. 60NANB10D267 and DTRA Grant No. HDTRA1-10-1-0046. This material is based upon work supported as a part of the Center for Excitonics, as an Energy Frontier Research Center funded by the U.S. Department of Energy, Office of Science, Office of Basic Energy Sciences under Award number DESC0001088. AE acknowledges financial support from the DFG under Contract No. Ei 872/1-1. The work at MIT Lincoln

Parameter	FMO model	Quantum simulator
decay time (T_1)	\approx ns	\approx 10 μ s
average exciton transfer time	\approx 5 ps	\approx 25 ns
decay time between the exciton states	\approx ps	\approx 5 ns
dephasing in exciton manifold	\approx 100 fs	\approx 500 ps
time scale of quantum beatings (τ_{osc})	\approx 200 fs	\approx 1 ns
coupling between sites	\approx 10 cm^{-1} - 122 cm^{-1}	\approx 60 MHz - 730 MHz
relative static site energy shifts	\approx 10 cm^{-1} - 500 cm^{-1}	\approx 60 MHz - 3 GHz
temperature	300 K	60 mK

TABLE I. Comparison of parameters for the FMO complex and the quantum simulator. The timescales shown below are for the dressed states of flux qubits coupled to the quantum harmonic oscillators. For more details see Figure S3 and Tables S1, S2, and S3 in the Supporting Information. Notice that the decay time in a single qubit (T_1) does not need to be mapped directly from the FMO dynamics. With nowadays achievable decay times in superconducting qubits, which are 3 orders of magnitude larger than the excitation transfer time between the qubits, the dynamics of the FMO complex can be simulated.

Laboratory is sponsored by the United States Air Force under Air Force Contract No. FA8721-05-C-0002. Opinions, interpretations, recommendations and conclusions

are those of the authors and are not necessarily endorsed by the United States Government.

* aspuru@chemistry.harvard.edu

-
- [1] I. Kassal *et al.*, *Simulating chemistry using quantum computers*, Annu. Rev. Phys. Chem. 62 (2011), pp. 185–207.
- [2] R. P. Feynman, *Quantum mechanical computers*, Found. Phys. 16 (1982), pp. 507; *Simulating physics with computers*, Int. J. Theor. Phys. 21 (1986), pp. 467.
- [3] M. A. Nielsen and I. L. Chuang, *Quantum computation and quantum information* (Cambridge, 2000).
- [4] D. P. DiVincenzo, *The physical implementation of quantum computation*, Fortschritte der Physik 48 (2000), pp. 771–784; quant-ph/0002077.
- [5] I. Buluta, and F. Nori, *Quantum simulators*, Science 326 (2009), pp. 108–111.
- [6] A. Aspuru-Guzik, A. D. Dutoi, P. J. Love and M. Head-Gordon, *Simulated Quantum Computation of Molecular Energies* Science 309 (2005), pp. 1704.
- [7] R. Schützhold, and S. Mostame, *Quantum simulator for the $O(3)$ nonlinear sigma model*, JETP Lett. 82 (2005), pp. 248.
- [8] S. Mostame, and Ralf Schützhold, *Quantum simulator for the Ising model with electrons floating on a helium film*, Phys. Rev. Lett. 101 (2008), pp. 220501.
- [9] D. I. Tsomokos, S. Ashhab, and F. Nori, *Using superconducting qubit circuits to engineer exotic lattice systems*, Phys. Rev. A 82 (2010), pp. 052311.
- [10] E. J. Pritchett *et al.*, *Quantum simulation of molecular collisions with superconducting qubits*, arXiv:1008.0701 (2010).
- [11] G. S. Engel *et al.*, *Evidence for wavelike energy transfer through quantum coherence in photosynthetic systems*, Nature 446 (2007), pp. 782–786.
- [12] H. Lee, Y.-C. Cheng, and G. R. Fleming, *Coherence dynamics in photosynthesis: protein protection of excitonic coherence*, Science 316 (2007), pp. 1462–1465.
- [13] M. Cho, H. M. Vaswani, T. Brixner, J. Stenger, and G. R. Fleming, *Exciton analysis in 2D electronic spectroscopy*, J. Phys. Chem. B 109 (2005), pp. 10542–10556.
- [14] J. Adolphs, and T. Renger, *How proteins trigger excitation energy transfer in the FMO complex of green sulfur bacteria*, Biophys. J. 91 (2006), pp. 2778–2797.
- [15] F. Müh *et al.*, *Alpha-helices direct excitation energy flow in the Fenna-Matthews-Olson protein*, Proc. Natl. Acad. Sci. 104 (2007), pp. 16862–16867.
- [16] P. Rebentrost, M. Mohseni, I. Kassal, S. Lloyd and A. Aspuru-Guzik, *Environment-assisted quantum transport*, New J. Phys. 11 (2009), pp. 033003.
- [17] P. Rebentrost, M. Mohseni, and A. Aspuru-Guzik, *Role of quantum coherence in chromophoric energy transport*, J. Phys. Chem. B 113 (2009), pp. 9942–9947.
- [18] F. Caruso *et al.*, *Highly efficient energy excitation transfer in light-harvesting complexes: The fundamental role of noise-assisted transport*, J. Chem. Phys. 131 (2009), pp. 105106.
- [19] B. Palmieri, D. Abramavicius, and S. Mukamel, *Lindblad equations for strongly coupled populations and coherences in photosynthetic complexes*, J. Chem. Phys. 130 (2009), pp. 204512.
- [20] A. Ishizaki, and G. R. Fleming, *Theoretical examination of quantum coherence in a photosynthetic system at physiological temperature*, Proc. Natl. Acad. Sci. 106 (2009), pp. 17255–17260.
- [21] M. Sarovar, A. Ishizaki, G. R. Fleming, and K. B. Whaley, *Quantum entanglement in photosynthetic light-harvesting complexes*, Nature Phys. 6 (2010), pp. 462–467.
- [22] P. Rebentrost, and A. Aspuru-Guzik, *Communication: Exciton-phonon information flow in the energy transfer process of photosynthetic complexes*, J. Chem. Phys. 134 (2011), pp. 101103.
- [23] M. S. am Busch, F. Müh, M. El-Amine Madjet, and T. Renger, *The eighth bacteriochlorophyll completes the excitation energy funnel in the FMO protein*, J. Phys. Chem. Lett 2 (2011), pp. 93–98.
- [24] F. Verstraete, M. M. Wolf, and J. I. Cirac, *Quantum computation and quantum-state engineering driven by dissi-*

- pation, *Nature Physics* 5 (2009), pp. 633–636.
- [25] J. T. Barreiro *et al.*, *An open-system quantum simulator with trapped ions*, *Nature* 470 (2011), pp. 486–491.
- [26] L.-B. Yu *et al.*, *Simulation of the spin-boson model with superconducting phase qubit coupled to a transmission line*, arXiv:1012.5764 (2010).
- [27] A. O. Niskanen *et al.*, *Quantum coherent tunable coupling of superconducting qubit*, *Science* 316 (2007), pp. 723–726.
- [28] F. G. Paauw, A. Fedorov, C. J. P. M. Harmans, and J. E. Mooij, *Tuning the gap of a superconducting flux qubit*, *Phys. Rev. Lett.* 102 (2009), pp. 090501.
- [29] T. Hime *et al.*, *Solid-state qubits with current-controlled coupling*, *Science* 314 (2006), pp. 427–429.
- [30] A. G. Fowler *et al.*, *Long-range coupling and scalable architecture for superconducting flux qubits*, *Phys. Rev. B* 76 (2007), pp. 174507.
- [31] V. May, and O. Kühn, *Charge and energy transfer dynamics in molecular systems* (WILEY-VCH, 2004).
- [32] C. Olbrich, J. Strümpfer, K. Schulten, and U. Kleinekathöfer, *Quest for spatially correlated fluctuations in the FMO light-harvesting complex*, *J. Phys. Chem. B* 115 (2011), pp. 758–764.
- [33] S. Shim, P. Rebertus, S. Valleau and A. Aspuru-Guzik, *Atomistic study of the long-lived quantum coherences in the Fenna-Matthews-Olson complex*, *Biophysical Journal* 102 (2012), pp. 649–660.
- [34] A. J. Leggett *et al.*, *Dynamics of the dissipative two-state system*, *Rev. Mod. Phys.* 59 (1987), pp. 1–85.
- [35] S. A. Egorov, K. F. Everitt, J. L. Skinner, *Quantum dynamics and vibrational relaxation*, *J. Phys. Chem. A* 103 (1999), pp. 9494–9499.
- [36] G. Ritschel, J. Roden, W. T. Strunz, and A. Eisfeld *An efficient method to calculate excitation energy transfer in light harvesting systems: Application to the FMO complex*, *New J. Phys.* 13 (2011), pp. 113034.
- [37] H. Haken and P. Reineker, *The coupled coherent and incoherent motion of excitons and its influence on the line shape of optical absorption*, *Z. Physik.* 249 (1972), pp. 253–268; H. Haken and G. Strobl, *An exactly solvable model for coherent and incoherent exciton motion*, *Z. Physik.* 262 (1973), pp. 135–148.
- [38] M. Wendling *et al.*, *Electron-vibrational coupling in the Fenna-Matthews-Olson complex of *Prosthecochloris aestuarii* determined by temperature-dependent absorption and fluorescence line-narrowing measurements*, *J. Phys. Chem. B* 104 (2000), pp. 5825–5831.
- [39] J. Seibt *et al.*, *Vibronic transitions and quantum dynamics in molecular oligomers: A theoretical analysis with an application to aggregates of perylene bisimides*, *J. Phys. Chem. A* 113 (2009), pp. 13475–13482.
- [40] J. Strümpfer and K. Schulten, *Light harvesting complex II B850 excitation dynamics*, *J. Chem. Phys.* 131 (2009), pp. 225101.
- [41] C. Kreisbeck *et al.*, *High-performance solution of hierarchical equations of motions for studying energy-transfer in light-harvesting complexes*, *Journal of Chemical Theory and Computation* 7 (2011), pp. 2166.
- [42] C. Kreisbeck, T. Kramer, *Long-lived electronic coherence in dissipative exciton-dynamics of light-harvesting complexes*, arXiv:1203.1485 (2012).
- [43] J. Clarke, and F. K. Wilhelm, *Superconducting quantum bits*, *Nature* 453 (2008), pp. 1031–1042.
- [44] S. Ashhab *et al.*, *Interqubit coupling mediated by a high-excitation-energy quantum object*, *Phys. Rev. B* 77 (2008), pp. 014510.
- [45] I. Chiorescu, Y. Nakamura, C. J. P. M. Harmans, and J. E. Mooij, *Coherent quantum dynamics of a superconducting flux qubit*, *Science* 299 (2003), pp. 1869–1871.
- [46] A. N. Omelyanchouk *et al.*, *Noise-induced quantum coherence and persistent Rabi oscillations in a Josephson flux qubit*, *Phys. Rev. B* 80 (2009), pp. 212503.
- [47] H. B. Callen, and T. A. Welton, *Irreversibility and generalized noise*, *Phys. Rev.* 83 (1951), pp. 34–40.
- [48] F. K. Wilhelm, M. J. Storck, U. Hartmann, and M. R. Geller, *Superconducting qubits II: Decoherence*, cond-mat/0603637 (2006).
- [49] F. Caruso *et al.*, *Simulation of noise-assisted transport via optical cavity networks*, *Phys. Rev. A* 83 (2011), pp. 013811.
- [50] F. L. Semião, K. Furuya, G. J. Milburn, *Vibration-enhanced quantum transport*, *New J. Phys.* 12 (2010), pp. 083033.
- [51] J. Hauss *et al.*, *Single-qubit lasing and cooling at the Rabi frequency*, *Phys. Rev. Lett.* 100 (2008), pp. 037003.
- [52] P. Bertet *et al.*, *Dephasing of a superconducting qubit induced by photon noise*, *Phys. Rev. Lett.* 95 (2005), pp. 257002.
- [53] P. Bertet *et al.*, *Dephasing of a flux qubit coupled to a harmonic oscillator*, arXiv:cond-mat/0507290 (2005).
- [54] M. Steffen *et al.*, *High-coherence hybrid superconducting qubit*, *Phys. Rev. Lett.* 105 (2010), pp. 100502.
- [55] H. Mori, *A continued-fraction representation of the time-correlation functions*, *Progress of Theoretical Physics* 34 (1965), pp. 399–416.
- [56] K. H. Hughes, C. D. Christ, and I. Burghardt, *Effective-mode representation of non-Markovian dynamics: a hierarchical approximation of the spectral density. I. Application to single surface dynamics*, *J. Chem. Phys.* 131 (2009), pp. 024109.
- [57] J. Prior *et al.*, *Efficient simulation of strong system-environment interactions*, *Phys. Rev. Lett.* 105 (2010), pp. 050404.
- [58] F. Yoshihara *et al.*, *Decoherence of flux qubits due to $1/f$ flux noise*, *Phys. Rev. Lett.* 97 (2006), pp. 167001.

I. SUPPORTING INFORMATION

II. COORDINATE REPRESENTATION OF THE MODEL HAMILTONIAN

In this section we derive the model Hamiltonian of a single molecule (Eq. [1] in the main article for $N = 1$) from the Born-Oppenheimer approximation. Restricting to two electronic states, the ground state $|g\rangle$ and the excited state $|e\rangle$, the Hamiltonian in the Born-Oppenheimer approximation is [1]:

$$H = H_{\text{nuc,g}}(R)|g\rangle\langle g| + H_{\text{nuc,e}}(R)|e\rangle\langle e|, \quad (1)$$

where R describes the collection of $3N_{\text{nuc}}$ modes relevant to the molecule (both local and protein modes), $R = \{R_1, \dots, R_{3N_{\text{nuc}}}\}$, with N_{nuc} being the number of nuclei. The Hamiltonians $H_{\text{nuc,g/e}}(R)$ describe the kinetic and potential energy of the nuclei, T_{nuc} and V_{nuc} , respectively: $H_{\text{nuc,g/e}}(R) = T_{\text{nuc}} + V_{\text{nuc,g/e}}(R)$. The potential energy is given by $V_{\text{nuc,g/e}}(R) = V_{\text{nuc-nuc}}(R) + E_{\text{g/e}}(R)$ with the inter-nuclear potential energy $V_{\text{nuc-nuc}}$ and the potential energy due to the electrons $E_a(R)$. We assume a displaced harmonic oscillator model for the potential of ground and excited state:

$$V_{\text{nuc,g}}(q) = U_g + \sum_{i=1}^{3N_{\text{nuc}}} \frac{\hbar\omega_i}{2} q_i^2, \quad (2)$$

$$V_{\text{nuc,e}}(q) = U_e + \sum_{i=1}^{3N_{\text{nuc}}} \frac{\hbar\omega_i}{2} (q_i - d_i)^2. \quad (3)$$

Here, we introduced the renormalized coordinates $q = R - R_0$, where R_0 are the equilibrium positions in the electronic ground state (minimum of the ground state potential energy surface). The respective energies of the electronic states at the minimum of the respective potentials are U_g and U_e . We have assumed that the frequency ω_i of mode i remains unchanged in the excited state. The displacement of the i th mode in the excited state is given by d_i . The q -dependent energy gap is given by the difference of the two potentials:

$$V_{\text{nuc,e}}(q) - V_{\text{nuc,g}}(q) = \Delta U + \sum_{i=1}^{3N_{\text{nuc}}} \frac{\hbar\omega_i}{2} d_i^2 - \sum_{i=1}^{3N_{\text{nuc}}} \hbar\omega_i d_i q_i,$$

where the first term $\Delta U = U_e - U_g$ is the energy difference between the potential minima of ground and excited state. The second term gives the reorganization energy:

$$\lambda = \sum_i \lambda_i = \sum_i \frac{\hbar\omega_i}{2} d_i^2. \quad (4)$$

The third term gives the linear dependence of the gap on the coordinates of the harmonic oscillator, and is the exciton-vibrational coupling term. The total Hamilto-

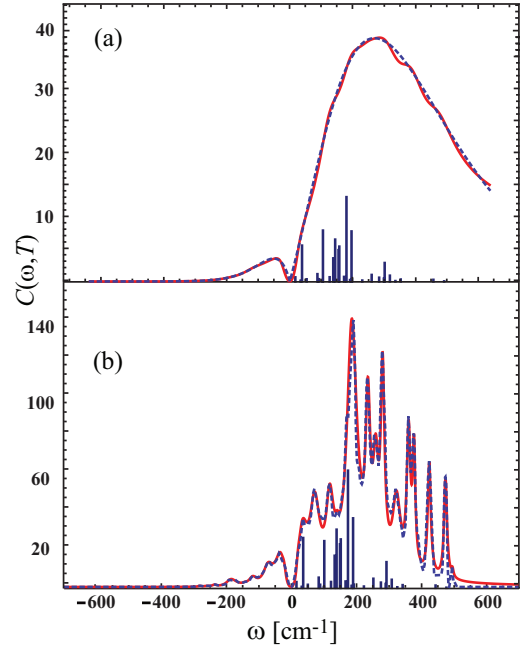


FIG. 1. The parametrization of the temperature-dependent (a) super-Ohmic mode density and (b) experimental [2] mode density of the FMO complex into distinct quantum oscillators. The blue dashed lines are the mode densities and the red solid lines are accurate simulation with LRC-oscillators coupled to the flux qubits, see Figure 1 (a) of the main article. The temperature for both mode densities is 77 [K]. The super-Ohmic mode density is simulated with 7 damped LRC-oscillators and the experimental one is simulated with 15 damped oscillators. The blue bars show the transition energies [3] for the FMO complex.

nian in the harmonic approximation is thus:

$$H_{\text{tot}} = \underbrace{\left(\Delta U + \sum_i \lambda_i \right)}_{H_{\text{el}}} |e\rangle\langle e| + \underbrace{\left(T_{\text{nuc}} + \sum_i \frac{\hbar\omega_i}{2} q_i^2 \right)}_{H_{\text{ph}}} \mathbf{1} + \underbrace{\sum_i \hbar\omega_i d_i q_i}_{H_{\text{el-ph}}} |e\rangle\langle e|. \quad (5)$$

Here we defined the respective Hamiltonians for the electronic system, phonon bath and electron-phonon coupling, H_{el} , H_{ph} , and $H_{\text{el-ph}}$. The system identity operator is given by $\mathbf{1} = |g\rangle\langle g| + |e\rangle\langle e|$.

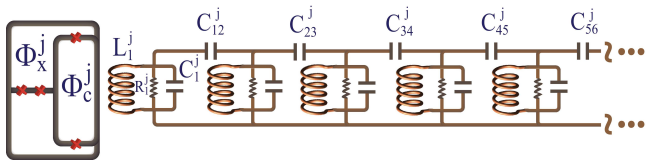


FIG. 2. The parallel combination of LRC oscillators shown in Figure. 2 (a) of the main article can be mapped to a linear chain of oscillators, such that only a single resonator would need to be coupled directly to each qubit. The oscillators can be coupled, for example, capacitively via capacitors C_{mn}^j .

III. ENERGY TRANSFER PATHWAYS FOR THE FMO COMPLEX

We briefly explain the red arrows in Figure 1 (b), which show schematically the downwards energy transfer pathways for the FMO complex, similar to Ref. [4] which considered seven-site model for the FMO complex.

From a system-bath model like Eq. (1) (main article), one can derive a master equation for the density matrix by using, for example, Redfield theory with the secular approximation [5]. Redfield theory assumes weak coupling and a Markovian bath. This leads to decoherence rates in the energy basis between energy states M and N given by [3] (without loss of generality $\hbar\omega_{MN} = E_M - E_N > 0$):

$$\Gamma_{MN}^\uparrow = 2\pi\gamma_{MN}J(\omega_{MN})n(\omega_{MN}), \quad (6)$$

$$\Gamma_{MN}^\downarrow = 2\pi\gamma_{MN}J(\omega_{MN})[n(\omega_{MN}) + 1]. \quad (7)$$

Here, Γ_{MN}^\uparrow (Γ_{MN}^\downarrow) is the rate up (down) in energy and $n(\omega_{MN})$ is the mean number of vibrational quanta with energy $\hbar\omega_{MN}$ that are excited at a given temperature T :

$$n(\omega_{MN}) = 1/[\exp(\hbar\omega_{MN}/k_B T) - 1]. \quad (8)$$

The factor $\gamma_{MN} = \sum_j |\langle M|j\rangle|^2 |\langle j|N\rangle|^2$ arises from the basis transformation between site and energy basis. In Figure 1 (a), the red arrows show a selected number of downward transitions with $\gamma_{MN}J(\omega_{MN}) \geq 0.3 \text{ cm}^{-1}$.

IV. ENVIRONMENT-ASSISTED QUANTUM TRANSPORT

Here we briefly discuss the main features of environment-assisted quantum transport and what is to be expected from an experiment scanning the ratio of dephasing rate over system energy scale. For the qubit system in our proposed quantum simulator, the couplings

and the differences in the qubit splittings give a general energy scale Λ . The site energy level fluctuations lead to pure dephasing as the dominant decoherence mechanism, which is phenomenologically characterized by a pure dephasing rate γ . In the active noise engineering case, each site is driven, for example, by white noise with an amplitude $\sqrt{\gamma}$. The amplitude can be easily tuned in the external noise generator. In the passive case, the noise level can be regulated by the temperature of the sample. For both cases, if the dephasing rate γ is much smaller than the energy scale Λ , quantum localization is predicted to arise from the disorder in the energy levels. This leads to a small population at the target site. Increasing the dephasing rate such that $\gamma \approx \Lambda$ is expected [7] to lead to an increased population at the target site. Finally, it is expected that for the dephasing rate $\gamma \gg \Lambda$ diminished population arrives at the target site, since quantum transport is suppressed by the Zeno effect.

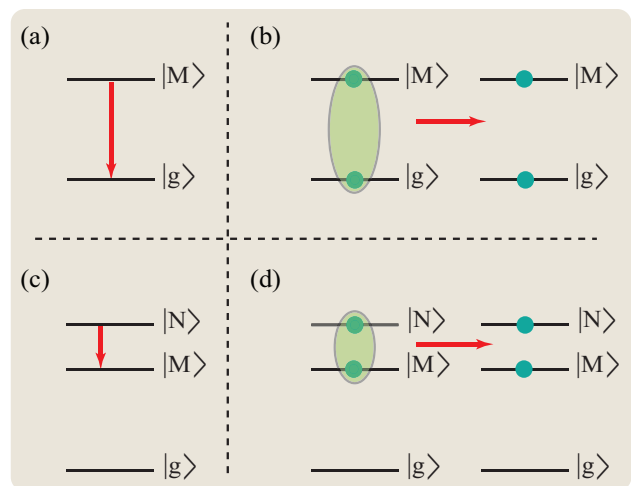


FIG. 3. Sketch of the basic processes in excitonic energy transfer. Confer to Table 1 in the main text (or Table S1) for numerical values of the time scales of the respective processes. Let $|g\rangle$ be the electronic ground state and $|M\rangle$ and $|N\rangle$ be two delocalized electronic excited states. (a) Decay with the *decay time* T_1 (Another name for this process is exciton recombination). (b) Dephasing of a superposition between ground state and an excited state. This process usually happens on a very fast time scale and is not relevant for the present discussion. (c) Decay in the single exciton manifold without the loss of the excitation to the ground state, characterized by the *decay time between exciton states*. (d) Dephasing in the single exciton manifold. Consider a superposition of exciton states $|\psi\rangle = \frac{1}{\sqrt{2}}(|M\rangle + |N\rangle)$. Then this dephasing process causes the initial density matrix $|\psi\rangle\langle\psi|$ to decay to an equal mixture $1/2(|M\rangle\langle M| + |N\rangle\langle N|)$ at long times. The time scale of this process is characterized by the *dephasing time in the single exciton manifold*.

-
- [1] V. May, and O. Kühn, *Charge and energy transfer dynamics in molecular systems* (WILEY-VCH, 2004).
- [2] M. Wendling, T. Pullerits, M. A. Przyjalowski, S. I. E. Vulto, T. J. Aartsma, R. van Grondelle, H. van Amerongen, *Electron-vibrational coupling in the Fenna-Matthews-Olson complex of Prosthecochloris aestuarii determined by temperature-dependent absorption and fluorescence line-narrowing measurements*, J. Phys. Chem. B 104 (2000), pp. 5825–5831.
- [3] J. Adolphs, and T. Renger, *How proteins trigger excitation energy transfer in the FMO complex of green sulfur bacteria*, Biophys. J. 91 (2006), pp. 2778–2797.
- [4] T. Brixner, J. Stenger, H. M. Vaswani, M. Cho, R. E. Blankenship, and G. R. Fleming, *Two-dimensional spectroscopy of electronic couplings in photosynthesis*, Nature 434 (2005), pp. 625–628.
- [5] H. P. Breuer, F. Petruccione, *The theory of open quantum systems* (Oxford, 2002).
- [6] G. Panitchayangkoon, D. Hayes, K. A. Fransted, J. R. Caram, E. Harel, J. Wen, R. E. Blankenship, and G. S. Engel, *Long-lived quantum coherence in photosynthetic complexes at physiological temperature*, Proc. Natl. Acad. Sci. 107 (2010), pp. 16862–16867.
- [7] P. Rebentrost, M. Mohseni, I. Kassal, S. Lloyd and A. Aspuru-Guzik, *Environment-assisted quantum transport*, New J. Phys. 11 (2009), pp. 033003.

Parameter	FMO model	Quantum simulator
decay time (\mathbb{T}_1) (single site electron-hole recombination)	\approx ns	\approx 10 μ s
average exciton transfer time (from site 8 to site 3)	\approx 5 ps	\approx 25 ns
decay time between the exciton states (jump between exciton states)	\approx ps	\approx 5 ns
dephasing in exciton manifold (pure dephasing)	\approx 100 fs	\approx 500 ps
time scale of quantum beatings (τ_{osc})	\approx 200 fs	\approx 1 ns
coupling between sites	\approx 10 cm^{-1} - 122 cm^{-1}	\approx 60 MHz - 730 MHz
relative static site energy shifts $ \tilde{\epsilon}_i - \tilde{\epsilon}_j \equiv \Delta_i - \Delta_j $	\approx 10 cm^{-1} - 500 cm^{-1}	\approx 60 MHz - 3 GHz
dynamic fast fluctuations [6] (dephasing rate)	\approx 250 \pm 100 cm^{-1} at 300 K \approx 40 \pm 10 cm^{-1} at 77 K	\approx 1.5 GHz \pm 600 MHz \approx 240 MHz \pm 60 MHz
temperature	300 K \approx 208 cm^{-1} 100 K \approx 69.5 cm^{-1} 77 K \approx 53 cm^{-1}	60 mk \approx 1.2 GHz 20 mk \approx 417 MHz 15 mk \approx 317 MHz

TABLE I. Comparison of parameters for the FMO complex and the quantum simulator. The timescales shown below are for the dressed states of flux qubits coupled to the quantum harmonic oscillators. Notice that the decay time in a single qubit (\mathbb{T}_1) does not need to be mapped directly from the FMO dynamics. With nowadays achievable decay times in superconducting qubits, which are 3 orders of magnitude larger than the excitation transfer time between the qubits, the dynamics of the FMO complex can be simulated.

FMO complex

	transition frequency	coupling strength	quality factor
oscillator No. 1	$\approx 27 \text{ cm}^{-1}$	$\approx 2.42 \text{ cm}^{-1}$	≈ 0.67
oscillator No. 2	$\approx 74 \text{ cm}^{-1}$	$\approx 8.60 \text{ cm}^{-1}$	≈ 0.49
oscillator No. 3	$\approx 140 \text{ cm}^{-1}$	$\approx 11.98 \text{ cm}^{-1}$	≈ 0.47
oscillator No. 4	$\approx 246 \text{ cm}^{-1}$	$\approx 14.10 \text{ cm}^{-1}$	≈ 0.80
oscillator No. 5	$\approx 380 \text{ cm}^{-1}$	$\approx 10.00 \text{ cm}^{-1}$	≈ 1.27
oscillator No. 6	$\approx 560 \text{ cm}^{-1}$	$\approx 5.40 \text{ cm}^{-1}$	≈ 1.84

Quantum simulator

	transition frequency	coupling strength	quality factor
oscillator No. 1	$\approx 162 \text{ MHz}$	$\approx 14.50 \text{ MHz}$	≈ 0.67
oscillator No. 2	$\approx 444 \text{ MHz}$	$\approx 51.56 \text{ MHz}$	≈ 0.49
oscillator No. 3	$\approx 839 \text{ MHz}$	$\approx 71.83 \text{ MHz}$	≈ 0.47
oscillator No. 4	$\approx 1.5 \text{ GHz}$	$\approx 84.54 \text{ MHz}$	≈ 0.80
oscillator No. 5	$\approx 2 \text{ GHz}$	$\approx 59.95 \text{ MHz}$	≈ 1.27
oscillator No. 6	$\approx 3 \text{ GHz}$	$\approx 32.38 \text{ MHz}$	≈ 1.84

TABLE II. Decomposition of the temperature-dependent super-Ohmic mode density at 300 K shown in Figure 4 (a) of the main article and simulation with 6 LRC-oscillators coupled to each flux qubit, see Figure 2 (a) of the main article.

FMO complex

	transition frequency	coupling strength	quality factor
oscillator No. 1	$\approx 20 \text{ cm}^{-1}$	$\approx 3.0 \text{ cm}^{-1}$	≈ 0.93
oscillator No. 2	$\approx 37 \text{ cm}^{-1}$	$\approx 5.9 \text{ cm}^{-1}$	≈ 1.35
oscillator No. 3	$\approx 72 \text{ cm}^{-1}$	$\approx 9.7 \text{ cm}^{-1}$	≈ 1.89
oscillator No. 4	$\approx 118 \text{ cm}^{-1}$	$\approx 7.8 \text{ cm}^{-1}$	≈ 4.00
oscillator No. 5	$\approx 142 \text{ cm}^{-1}$	$\approx 2.8 \text{ cm}^{-1}$	≈ 9.00
oscillator No. 6	$\approx 190 \text{ cm}^{-1}$	$\approx 16.5 \text{ cm}^{-1}$	≈ 5.00
oscillator No. 7	$\approx 237 \text{ cm}^{-1}$	$\approx 10.4 \text{ cm}^{-1}$	≈ 8.80
oscillator No. 8	$\approx 260 \text{ cm}^{-1}$	$\approx 6.1 \text{ cm}^{-1}$	≈ 10.80
oscillator No. 9	$\approx 282 \text{ cm}^{-1}$	$\approx 9.9 \text{ cm}^{-1}$	≈ 11.75
oscillator No. 10	$\approx 325 \text{ cm}^{-1}$	$\approx 4.8 \text{ cm}^{-1}$	≈ 18.06
oscillator No. 11	$\approx 363 \text{ cm}^{-1}$	$\approx 6.3 \text{ cm}^{-1}$	≈ 20.17
oscillator No. 12	$\approx 380 \text{ cm}^{-1}$	$\approx 5.3 \text{ cm}^{-1}$	≈ 29.23
oscillator No. 13	$\approx 426 \text{ cm}^{-1}$	$\approx 4.4 \text{ cm}^{-1}$	≈ 30.43
oscillator No. 14	$\approx 478 \text{ cm}^{-1}$	$\approx 3.4 \text{ cm}^{-1}$	≈ 48.00
oscillator No. 15	$\approx 500 \text{ cm}^{-1}$	$\approx 1.3 \text{ cm}^{-1}$	≈ 35.71

Quantum simulator

	transition frequency	coupling strength	quality factor
oscillator No. 1	$\approx 120 \text{ MHz}$	$\approx 18.00 \text{ MHz}$	≈ 0.93
oscillator No. 2	$\approx 222 \text{ MHz}$	$\approx 35.38 \text{ MHz}$	≈ 1.35
oscillator No. 3	$\approx 432 \text{ MHz}$	$\approx 58.16 \text{ MHz}$	≈ 1.89
oscillator No. 4	$\approx 707 \text{ MHz}$	$\approx 46.77 \text{ MHz}$	≈ 4.00
oscillator No. 5	$\approx 851 \text{ MHz}$	$\approx 16.79 \text{ MHz}$	≈ 9.00
oscillator No. 6	$\approx 1.1 \text{ GHz}$	$\approx 98.93 \text{ MHz}$	≈ 5.00
oscillator No. 7	$\approx 1.4 \text{ GHz}$	$\approx 62.36 \text{ MHz}$	≈ 8.80
oscillator No. 8	$\approx 1.6 \text{ GHz}$	$\approx 36.57 \text{ MHz}$	≈ 10.80
oscillator No. 9	$\approx 1.7 \text{ GHz}$	$\approx 59.36 \text{ MHz}$	≈ 11.75
oscillator No. 10	$\approx 1.9 \text{ GHz}$	$\approx 28.78 \text{ MHz}$	≈ 18.06
oscillator No. 11	$\approx 2.2 \text{ GHz}$	$\approx 37.77 \text{ MHz}$	≈ 20.17
oscillator No. 12	$\approx 2.3 \text{ GHz}$	$\approx 31.79 \text{ MHz}$	≈ 29.23
oscillator No. 13	$\approx 2.6 \text{ GHz}$	$\approx 26.38 \text{ MHz}$	≈ 30.43
oscillator No. 14	$\approx 2.9 \text{ GHz}$	$\approx 20.39 \text{ MHz}$	≈ 48.00
oscillator No. 15	$\approx 3 \text{ GHz}$	$\approx 7.79 \text{ MHz}$	≈ 35.71

TABLE III. Decomposition of the temperature-dependent experimental [2] mode density at 300 K shown in Figure 4 (b) of the main article and simulation with 15 LRC-oscillators coupled to each flux qubit, see Figure 2 (a) of the main article.